

Paper NA

Pierre

February 24, 2017

1 Introduction

The North American continent consists of an ancient cratonic core, formed during the Archean, that has not been subjected to orogeny for at least 1.8 Ga, bordered to the southeast and east, by progressively younger, stable, Proterozoic provinces (Hoffman 1988). In the west, the Rocky Mountain Front (RMF) separates the Proterozoic and Archean shield from younger, tectonically active provinces (Fig. 1). This relatively regular configuration makes North America an ideal target for seismic tomography, to investigate the relationship of lithospheric and asthenospheric structure to the geological features observed at the surface.

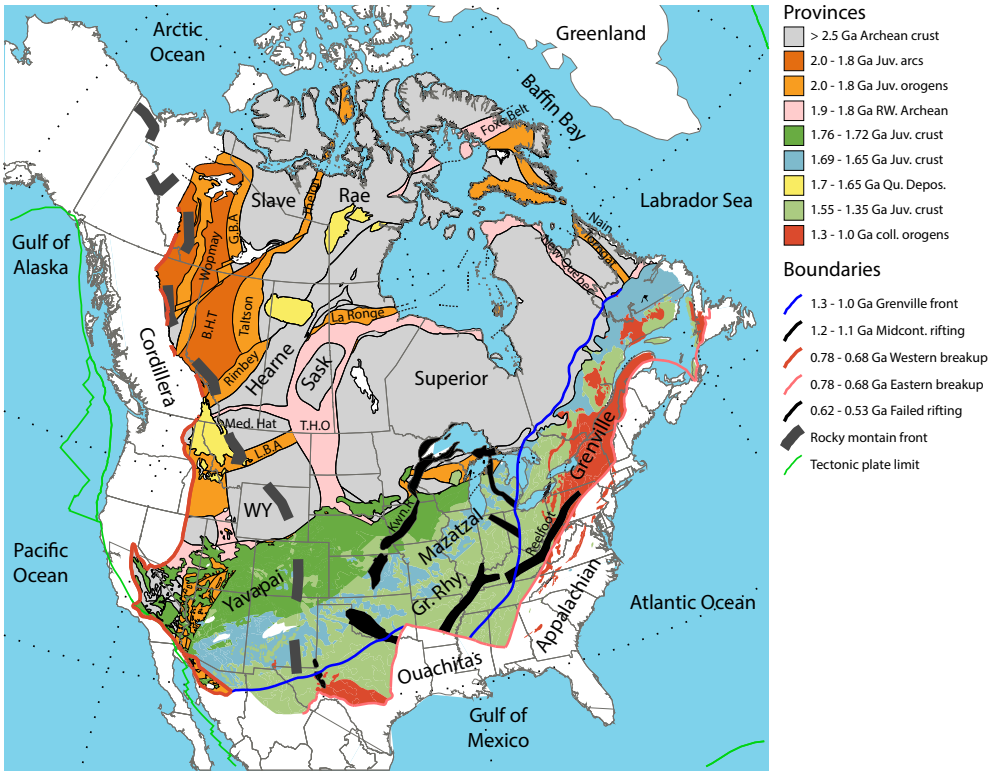


Figure 1: Large scale Precambrian architecture of North America (modified from Whitmeyer and Karlstrom (2007)). Colours indicate ages of different regions, as shown in the legend. The stable cratonic core is defined by the Rocky Mountain Front to the west (dashed dark grey line), defined by the surface trace of deformation), and the appalachian front to the east (solid light red line). The solid blue line demarcates the westward extent of the Grenville/Llano Front. The solid red line along the Cordillera province demarcates the breakup of Rodinia. Solid green lines indicate tectonic plate boundaries. Abbreviations are as follows: RW, re-worked; GBA, Great Bear Arc; BHT, Buffalo Head Terrane; Talston, Talston Arc; Rimbev, Rimbev Arc; Tornagat, Tornagat Arc; L.B.A, Little Belt Arc; LRA; THO, Trans-Hudson Orogen; RGR, Rio Grande Rift; Reelfoot, Reelfoor Rift; Kwn.R, Kewanowan Rift; Sask, Sask Craton; WY, Wyoming Province; Med. Hat., Medicine Hat Block; Grt. Rhy, GraniteRhyolite Province; Grenville, Grenville Province.

Differences in the seismic velocity structure between the craton and the western US extending down to at least 200 km were established already in the 1960's and 70's from the first studies of teleseismic P and S wave travel time anomalies (e.g. Cleary and Hales 1966, Herrin and Taggart 1968, Poupinet 1979), the first tomographic images based on P and S travel times (Romanowicz 1979) and long period surface waveforms (Woodhouse and Dziewonski 1984), as well as contrasted velocity-depth profiles obtained from the modeling of shear body waveforms at relatively short distances (e.g. Grand and Helmberger 1984). More recent body wave tomographic models have added considerable details to these images (Sigloch 2011, Burdick et al. 2014, Porritt et al. 2014; 2015)

Lateral variations in absolute velocities can be inferred from shear wave tomography, at scales from global (e.g. Su et al. 1994, Mégnin and Romanowicz 2000, Shapiro and Ritzwoller 2002, Panning and Romanowicz 2006, Kuszowski et al. 2008, Ritsema et al. 2010, Lekić and Romanowicz 2011, Debayle and Ricard 2012, Schaeffer and Lebedev 2013) to continental (van der Lee and Frederiksen 2005, Yuan et al. 2011; 2014, Schaeffer and Lebedev 2014). These studies confirm the presence of strong lateral variations in the thickness of the lithosphere across the RMF, with lithospheric roots extending

down to 200-250 km under the craton, thinning abruptly to the west to less than 80-100 km. This is also found from azimuthal anisotropy tomography, where a change in the anisotropy fast axis direction across the lithosphere-asthenosphere boundary (LAB) (Marone and Romanowicz 2007, Yuan and Romanowicz 2010).

While the mechanism of craton formation is still widely debated (e.g. King 2005, Lee et al. 2011), the presence of finer scale lateral and depth variations ([cite some body wave tomography studies](#) in seismic structure suggest a complex history. Moreover, studies of azimuthal anisotropy have shown the presence of laterally varying layering within the cratonic lithosphere (e.g. Levin et al. 1999, Deschamps et al. 2008, Yuan and Romanowicz 2010), which may indicate different modes and/or times of formation of the top c.a. 100 km of this lithosphere. Fine scale studies of converted and reflected phases indicate the presence of a sharp mid-lithospheric discontinuity (MLD) within the craton, marking the top of a mid-lithospheric low velocity zone (Thybo and Perchu 1997, Bostock 1998, Abt et al. 2010, Fischer et al. 2010, Rader et al. 2015, Ford et al. 2016) and even possibly several mid-lithospheric discontinuities (Calò et al. 2016). In addition, there is evidence from radially anisotropic shear wave tomography for separation between blocks of different

crustal ages extending to depths of at least 150 km (e.g. Yuan et al. 2014).

Much of this finer scale structure has been resolved owing to the availability of data from the dense broadband USArray TA deployment. With the completion of the coverage of the conterminous US, as well as availability of data from Canada and Greenland, it is now possible to further refine shear wave tomographic images of North America, and in particular of the stable Proterozoic and Archean provinces, to try and improve our understanding of the different stages of formation of the continent. It is also an unprecedented opportunity to experiment with improved waveform-based tomographic techniques.

In a previous study, we presented a radially anisotropic shear velocity model of the North American upper mantle based on a combination of long period teleseismic and regional waveform data (Yuan et al. 2014). The regional waveform data (down to 40 s period) were, for the first time at this scale, compared to 3D synthetics computed using RegSEM (Cupillard et al. 2012), a Spectral Element Method (SEM) code suitable for continental-scale wavefield computations. Due to the very heavy computations that would have been necessary to compute the predicted teleseismic wavefield numerically at each iteration of the inversion, the latter was, instead, computed

using Non-Linear Assymptotic Coupling Theory (NACT, Li and Romanowicz 1995), a methodology based on normal mode perturbation theory, that is computationally more efficient (albeit approximate), and has been used in the development of several generations of global and continental scale shear velocity models based on time-domain waveform inversion (Li and Romanowicz 1996, Mégnin and Romanowicz 2000, Gung et al. 2003, Panning and Romanowicz 2006, Yuan et al. 2011)

The resulting 2014 model of North America presents some interesting features, in particular a correlation of radial anisotropy structure with lithospheric blocks corresponding to different orogenies in the eastern US and continental shelf. While more rigorous than inversions practiced by most groups and based on the path-average surface wave approximation (PAVA, Woodhouse and Dziewonski 1984), this mixed methodology nevertheless presents some inconsistencies from the theoretical point of view, since the predicted wavefield through the target model space is computed with different theories for teleseismic and regional distance data, respectively.

To better integrate teleseismic data into our regional tomographic inversions, we developed a general framework called "Box Tomography" (see Masson et al. 2013, Masson and Romanowicz 2016; 2017), that allow us to

consistently model and invert both teleseismic (i.e. associated with sources or receivers outside of the imaged region) and regional (i.e. associated with sources and receivers within the imaged region) waveform data using accurate numerical methods such as SEM. In Box Tomography, prior to the inversion, the seismic wavefield generated by teleseismic sources is first modeled numerically at the global scale for a given reference 3D model and is recorded at the surface of the region to be imaged. This reference wavefield is then used to construct virtual sources lying at the boundary of the regional modeling domain and reproducing the original wavefield as illustrated in Figure 4. Once the teleseismic sources have been moved (i.e. replaced by virtual sources) within the regional modeling domain, the tomographic inversion can be performed efficiently in a classical manner (i.e. using regional modeling only) as the teleseismic data are accounted for seamlessly thanks to the virtual sources. Related concepts have been proposed to account for teleseismic data in regional imaging (e.g. Wang et al., 2016 Monteiller et al., 2015), however, in these studies the global modeling of the reference wavefield is performed using a faster method that does not account for the effects induced by the 3D structure of the Earth outside the regional modeling domain. In this paper, we present the first application of Box Tomography to

continental scale waveform tomography in North America.

2 Methodology

Many studies have inverted for continental scale structure, in particular in North America, using fundamental mode and, in some cases, overtone surface wave dispersion data or waveforms observed at teleseismic distances. The usual practice is to first consider the best possible global scale tomographic shear wave velocity model, compute predictions of observables in this model using an approximate theory, generally the surface wave path average approximation (e.g. Nettles and Dziewoński 2008, Bedle and van der Lee 2009, Schaeffer and Lebedev 2014), or, in our group, NACT (Marone et al. 2007, Yuan et al. 2011). In the case when secondary observables such as dispersion data are considered, the contribution from outside of the target region is calculated once and for all in the background global model, and subtracted from the observed dispersion data. The resulting residual is attributed to structure in the target region and the tomographic inversion proceeds within this target model volume. When inverting waveforms, and in particular when a more accurate theory than the PAVA is considered,

such a simple procedure is not possible, and it is necessary to recompute the synthetic teleseismic waveforms, at each iteration, in a 3D model which is fixed outside of the target region, and updated only within it. This leads to substantial computations, even in the case of an approximate theory such as NACT, and becomes prohibitively expensive, if the 3D teleseismic wavefield is computed using SEM or another accurate numerical method, as especially as one aims to include increasingly shorter periods.

To overcome this problem, we take advantage of the "Box Tomography" theory which allows us to combine teleseismic and regional waveforms in a consistent manner to image regional targets at arbitrary locations. This general framework accommodates for arbitrary acquisition setups (i.e. with sources and receivers located outside the regional imaging box), is compatible with most popular numerical methods such as SEM or FD, and can produce exact seismograms and sensitivity kernels (i.e. similar to those obtained when solving the problem globally). In this study, we limit ourselves to the situation where both regional and teleseismic events are employed but where all the seismic stations lie within the regional computational domain. Furthermore, we neglect some higher order scattering effects, as proposed by Masson and Romanowicz (2016). In this situation, Box Tomography is

particularly efficient, as the computational effort to account for teleseismic data in regional inversions is limited to a few global scale simulations that are done once and for all prior to the inversion. Masson and Romanowicz (2016) showed that this approach can produce accurate regional tomographic images even though the elastic structure outside the imaged region is neither fully known prior to the inversion, nor updated during the inversion.

Here, we apply this methodology to the case of teleseismic three component waveform data observed at stations within North America, combined with "regional" waveform data for which both earthquakes and stations are located within the target region. This is the first time this methodology is applied in practice, and this study represents a proof of concept for this approach. Adding teleseismic data allows better azimuthal coverage of the target region than can be achieved using only the regional dataset, and eventually provides for the inclusion of constraints from additional phases such as, for example, teleseismic SS phases reflected inside the target region.

2.1 Dataset and model parametrization

The dataset includes three component acceleration waveforms from 2860

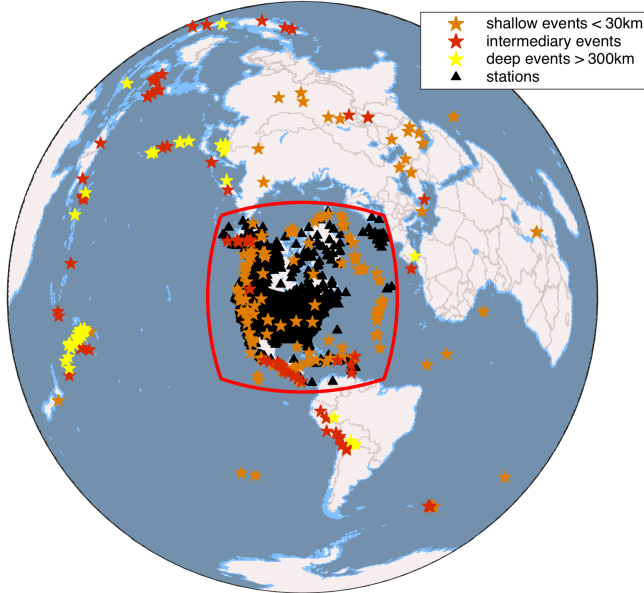


Figure 2: Source and station distribution for the new North American inversion. Black triangles show the seismic stations. Stars are 155 regional events, in addition to 122 teleseismic events. Orange stars indicate events shallower than 30km deep, Yellow stars for deeper than 300km and red one are in between. Thick red line indicates the boundaries used for the RegSEM forward simulation, which extends 89 by 89 horizontally and down to 1600 km and contains all stations and regional events.

permanent and temporary broadband stations located in the target region, a $89^\circ \times 89^\circ$ area encompassing most of north America (Figure 2). We considered two different datasets:

- a regional dataset consisting of 155 events ($4.5 < M_w < 6.0$) for which sources are located within the target region.

- a teleseismic dataset, consisting of 122 events ($5.5 < M_w < 6.9$) for which sources are located outside of the target region.

The waveforms are filtered between 40 and 400 s, with corner frequencies at 53 and 250 s, and windowed into wavepackets, according to the procedure of Li and Romanowicz (1996) ,allowing different weights to be applied according to relative amplitude of individual wavepackets, redundancy of paths and signal to noise ratio. This weighting step is crucial, as it homogenizes the data coverage within the region and provides a way to construct the data covariance matrix C_D , which we approximate as a diagonal matrix. At each iteration of the inversion, only those wavepackets are considered that satisfy predefined goodness of fit criteria compared to synthetics calculated in the current 3D model, in particular to avoid cycle slipping in our time domain waveform inversion procedure. As the model improves, at each iteration, additional wavepackets are included. The total number of wavepackets of fundamental and overtone Love and Rayleigh waves is given in Table 1, and provides a good coverage within the NA continent (Figure 3).

In addition to long period waveforms, we also consider a group velocity dispersion dataset (Shapiro and Ritzwoller 2002) provided in the form of $1^\circ \times 1^\circ$ maps between 25 and 100 s. The shorter periods (below 60 s) are

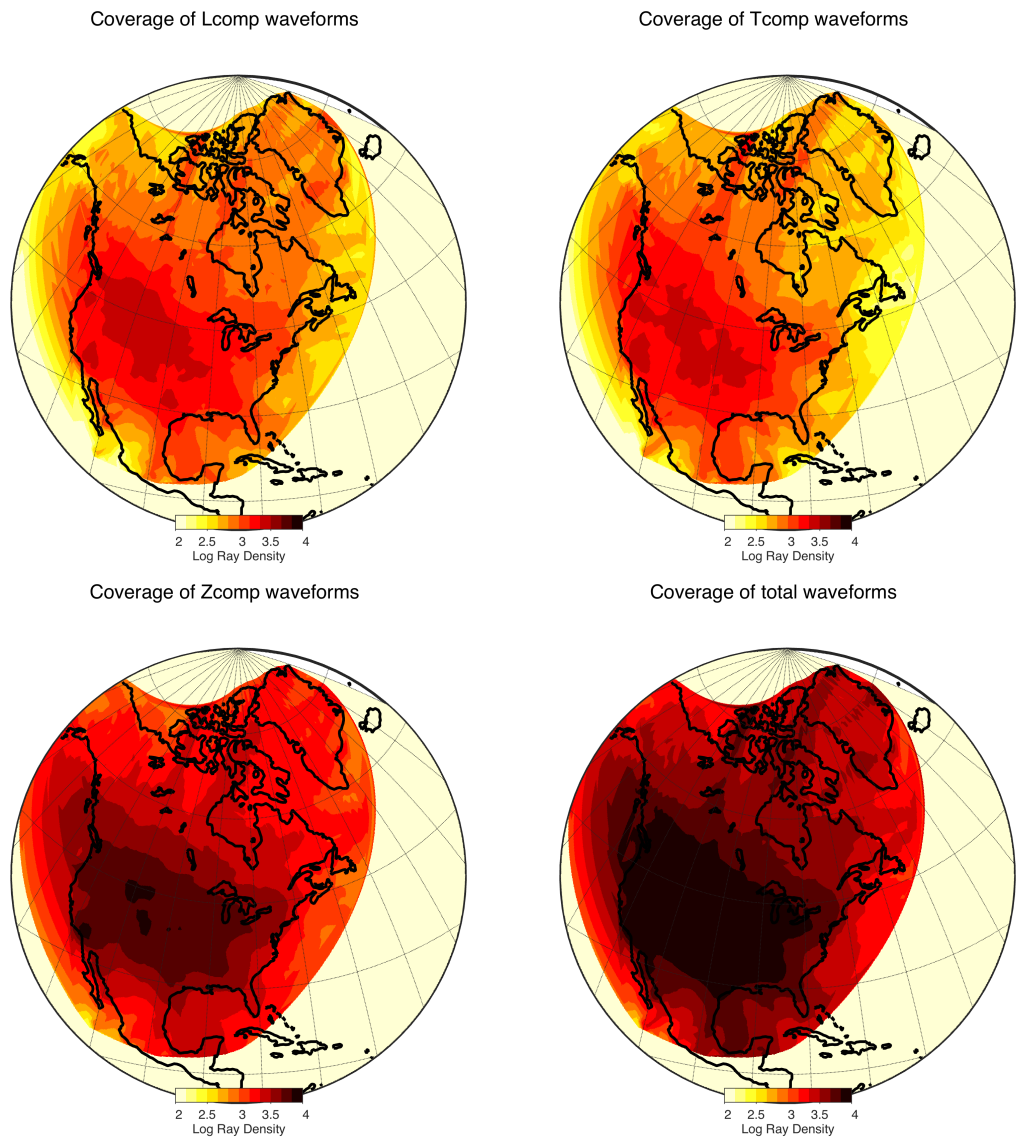


Figure 3: Density coverage for each component and all gathered.

used to constrain our homogenized crustal structure at each iteration, as described below, while the entire period range is included during the inversion for mantle structure, providing additional constraints for structure in the shallow parts of the mantle, that are consistent with the treatment of the crust.

As in our previous work at the global scale (French et al. 2013, French and Romanowicz 2014), we do not rely on an existing layered crustal model. There are several drawbacks to considering such models. First, they are constructed using data for limited regions that are then extrapolated to other regions based on a tectonic regionalization, and may not always fit real waveform data very well. Second, the inclusion of thin low velocity layers slows down the SEM computation significantly. Instead, we compute a radially anisotropic smooth crustal model on a $2^\circ \times 2^\circ$ grid through Monte Carlo Markov Chain (MCMC) simulation constrained by the group velocity dispersion data.

This process is called "homogenization" (e.g. Backus 1962, Capdeville and Marigo 2008), and yields a crustal model equivalent to a real crust within the period range of the data used to constrain it (i.e. here for periods longer than 20s). The thickness of the crust is a priori fixed to that of model

Crust2.0 (Bassin et al. 2000) when it is larger or equal to 30 km, and it is fixed at 30 km in regions where it is thinner. This results in a smooth, but realistic crust within most of the continent, and a crustal model that is not directly interpretable in the border regions of our model space (i.e. in the oceans and borders of the continent where the real crust is thin). We have shown that this does not bias the mantle structure imaged below 50 km (French and Romanowicz 2014). At each iteration of the inversion, we only invert for structure below 30 km depth, and subsequently recompute the crustal model for the next iteration by applying our MCMC approach with mantle structure fixed to that of the current iteration model. The procedure is described and discussed in detail in French and Romanowicz (2014)

Assuming that our azimuthal coverage is everywhere sufficient within our target region, we here solve only for radially anisotropic structure. If (A, C, F, L and N) are the 5 elastic parameters describing a radially anisotropic (or VTI) medium (Love 2013), then:

$$N = \rho V_{SH}^2, \quad L = \rho V_{SV}^2, \quad A = \rho V_{PH}^2, \quad C = \rho V_{PV}^2 \quad (1)$$

then the medium can equivalently be described by the 5 parameters ($V_S, V_P, \xi, \phi, \varepsilon$) where:

$$V_S = \sqrt{\frac{2V_{SV}^2 + V_{SH}^2}{3}} V_P = \sqrt{\frac{V_{PV}^2 + 4V_{PH}^2}{5}} \xi = \frac{N}{L}, \quad \varphi = \frac{C}{A}, \quad \eta = \frac{F}{A - 2L} \quad (2)$$

We only consider two of the 5 independent anisotropic parameters , those to which long period surface waveforms are the most sensitive: isotropic velocity V_S and the anisotropic parameter $\xi = \frac{V_{SH}^2}{V_{SV}^2}$, where V_{SH} is the velocity of waves polarized horizontally and V_{SV} that of waves polarized vertically . The other three parameters and density are constrained through empirical scaling relationships, following Montagner and Anderson (1989), and are based on laboratory measurements for upper mantle rocks.

The scaling parameters considered are (Montagner and Anderson 1989)

$$\frac{\delta(V_P)}{\delta(V_S)} = 0.5, \quad \frac{\delta(\rho)}{\delta(V_S)} = 0.33, \quad \frac{\delta(\eta)}{\delta(\xi)} = -2.5, \quad \frac{\delta(\varphi)}{\delta(\xi)} = -1.5, \quad (3)$$

We chose a parametrization in terms of V_S and ξ , rather than V_{SH} and V_{SV} , as this allows us to consider different spatial resolution and apply higher damping in the inversion to the less well resolved anisotropic parameter ξ , rather than having to reconstruct this parameter from differences in perturbations in the two quantities V_{SH} and V_{SV} , which would limit the resolution

allowed in isotropic velocity.

In previous studies (Marone and Romanowicz 2007, Yuan and Romanowicz 2010), after inverting for radial anisotropic structure (Marone et al. 2007, Yuan et al. 2011), we also inverted for azimuthal anisotropy, by adding constraints from SKS splitting measurements. This step will be the topic of a separate publication.

The target model space is geographically defined as shown in Figure 2, and is limited in depth down to 800 km. As in our previous tomographic studies, the model space is parametrized in terms of 26 cubic splines $\nu_q(r)$ vertically (Mégnin and Romanowicz 2000) from the core-mantle boundary to 30 km deep. Although we invert for structure only in the top 16 splines, corresponding to the top 700-800 km of the mantle. The spline nodes are spaced more closely at shallow depths, and located at the following radii: 5690, 5810, 5910, 5900, 6061, 6101, 6131, 6161, 6191, 6221, 6241, 6261, 6281, 6301, 6321, 6341 km. Laterally, we parametrize our model in terms of spherical splines $\beta(\theta, \phi)_p$ (Wang and Dahlen 1995). The combination of vertical and spherical splines constitutes a local basis for the description of smooth functions within the model volume. Thus, the value of a model parameter $m(r, \theta, \phi)$ can be computed at any point in space given the set of

spline coefficients m_{pq} :

$$m(\theta, \varphi, r) = \sum_p \sum_q m_{pq} \beta_p(\theta, \varphi) \nu_q(r) \quad (4)$$

The spherical spline parametrization has the advantage of allowing for variable grid parametrization, which can be adjusted according to data coverage (e.g. Marone et al. 2007). In our case, outside of the target region, we adopt a "level 6" spherical grid for V_S (2° knot spacing) and a "level 4" spherical grid for ξ (8° knot spacing), consistent with the parametrization of *SEMUCB_wm1* (French and Romanowicz 2014). Inside the well-sampled target region, we define a level 7 spherical grid (1° knot spacing) for V_S and level 6 (2° knot spacing) for ξ .

2.2 Forward modelling

During the inversion, all the synthetic seismograms are computed using the regional SEM code RegSEM (Cupillard et al. 2012) that takes into account effects of oceans, topography/bathymetry, ellipticity, and anelasticity, and where the limits of the computational domain are dealt with using absorbing boundaries. The synthetic seismograms associated with regional data (i.e. where both the seismic stations and the earthquake are located within the

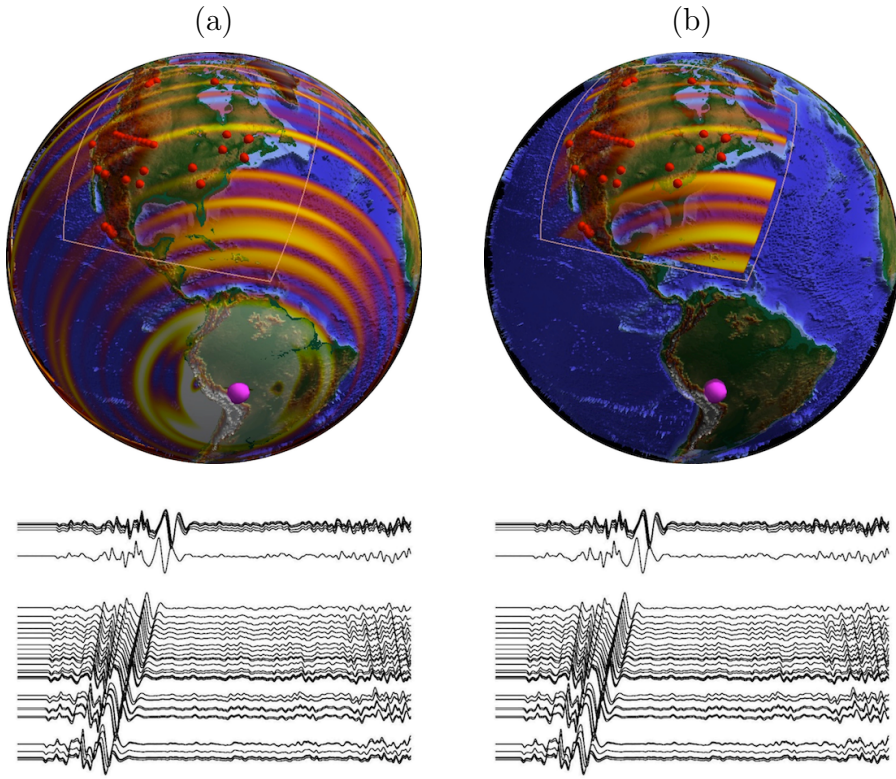


Figure 4: Comparison between a global scale simulation and a regional scale simulation of wave propagation following an earthquake in south America. The seismograms corresponds to the recordings at 37 station located in north America (red spheres). The pink sphere shows the epicenter of the earthquake. In (a), the wavefield is modeled globally using the spectral element method Specfem3D_globe (Komatitsch 2002). In (b), the wavefield is modeled regionally using the RegSEM. During the inversion, all the synthetic seismograms are computed using the regional SEM code RegSEM (Cupillard et al. 2012) code and regenerated thanks to virtual sources located around the computational domain (see Masson et al. 2013). The sismograms in (b) are exactly similar to those in (a), however, the computational effort is greatly reduced in the regional simulation (b).

regional modeling domain) do not require any specific treatment and are computed as in our previous studies using RegSEM (e.g. Yuan et al. 2014). The synthetic seismograms associated with teleseismic data (i.e. where the earthquake and the seismic stations are located outside and inside the regional modeling domain, respectively) are obtained using a two step procedure as proposed by Masson and Romanowicz (2016) as follows.

Prior to the inversion, the wavefields generated by teleseismic earthquakes are computed globally within our starting model (*SEMucb_wm1*) and a version of *SPECFEM3D_globe* (Komatitsch 2002) adapted to this model representation. During these global simulations, the 3 component displacement wavefield is recorded at a set of points with locations prescribed by the RegSEM code. Within the regional solver RegSEM, these points are the collocation or Gauss-Lobatto-Legendre (GLL) points belonging to the one element thick surface surrounding the regional modeling domain (see Masson et al. 2013). Note that our procedure does not require to store either the stress or the strain wavefield, which are computed naturally by the regional solver. This makes it easy to swap between different codes for modeling global seismic wave propagation (i.e. any code that outputs displacement seismograms can be used as such). Because the Courant criteria

which ensure the stability in SEM often lead to oversampling, we compress the recordings versus time using a least square B-spline transform (Unser et al. 1993a;b). We found this approach more efficient and practical than the more classic decimation/interpolation scheme. We typically achieve a data compression ratio of between 10 and 100 with no significant loss of accuracy. During the inversion, the global recordings are transformed to virtual sources that regenerate the global wavefield regionally. This operation is done on the fly by the RegSEM code.

Overall, the additional computational effort to account for teleseismic events consists of one global simulation per teleseismic event. These simulations are done once and for all before the inversion starts.

2.3 Inverse modelling

In continuity of our previous work (e.g Marone et al. 2007, Yuan et al. 2011; 2014), we use a hybrid iterative inversion scheme where, at each iteration, the forward wavefield is computed accurately using SEM, but the inverse step is solved using the formalism of Tarantola and Valette (1982) with sensitivity kernels calculated approximately using normal mode perturbation theory. This allows us to apply a fast converging Gauss-Newton quadratic optimiza-

tion scheme. As shown in Tarantola (2005), and in Appendix A of Lekić and Romanowicz (2011), it is far more important to use an accurate forward modelling scheme to compute the misfit function, provided of course that the theory captures the effects of the background long wavelength structure accurately (unlike the examples shown in Valentine and Trampert 2016). Inaccuracies in the theoretical treatment of kernels then result in smoothing errors that can be compensated for in subsequent iterations. In contrast, currently popular "adjoint tomographic" approaches (Zhu et al. 2015, Bozdağ et al. 2016) compute the numerically exact gradient, however, they also need to apply smoothing operators and regularization, which degrades the accuracy of their kernels. Importantly, they rely on a linear optimization scheme (conjugate gradient method), which is characterized by very slow convergence.

Our misfit function is defined in the time domain from the point by point differences between observed and synthetic waveforms as follows:

$$2\Phi(m_k) = [d - g(m_k)]^T C_d^{-1} [d - g(m_k)] + [m_p - m_k]^T C_m^{-1} [m_p - m_k] \quad (5)$$

where m_k represents the model estimate at the k-th iteration, d is the data vector (waveform discretized in time or group velocity as a function of period) and $g(m_k)$ is the corresponding discretized wavefield computed using SEM,

or the predicted group velocity dispersion. The model prior is m_p (i.e. the 3D starting model) and C_m and C_d represent a priori model and data covariance matrices, respectively. Minimizing Φ in the sense of the L2 norm leads to the equation for the k+1 model update:

$$m_{k+1} = m_k + (C_m G_k^T C_d^{-1} G_k + I)^{-1} (C_m G_k^T C^{-1} [d - g(m_k)] + m_p - m_k) \quad (6)$$

where G is the matrix of Frechet derivatives of $g(m)$ calculated at m_k . We compute G using NACT or PAVA, depending on the distance range of the corresponding source-station path. NACT and PAVA are both asymptotic (high frequency) approximations to first order normal mode perturbation theory. The PAVA includes along branch mode coupling only and is equivalent to the standard surface wave approximation (e.g Mochizuki 1986, Romanowicz 1987), as used for example in Woodhouse and Dziewonski (1984), in which a frequency shift and distance shift are introduced for each mode to account for the effects of heterogeneous structure. The corresponding kernels are "1D", i.e. they only depend on the average structure between the source and the receiver. This approximation is valid for single-mode seismograms, such as fundamental mode surface waves (e.g Romanowicz et al. 2008). NACT includes across branch-coupling, in addition to PAVA, which brings out 2D

sensitivity of waveforms in the vertical plane containing the source and the receiver. NACT breaks down when the distance between the source and station is short, so we compute kernels using NACT for epicentral distances larger than 15° , and PAVA for shorter distances. Neither PAVA nor NACT consider off-great circle plane sensitivity (i.e. focusing effects, e.g. Zhou et al. (2005)). These effects become important for accurate amplitude fitting. With our choice of misfit function, we are first and foremost fitting the phase, and for that, the 2D effects in the vertical plane are dominant, and important especially for overtones, as illustrated in Mégnin and Romanowicz (1999), Romanowicz et al. (2008).

3 Results

The tomographic inversion results for V_S and ξ are presented in figures ???. We divide the model description and interpretation into two parts, focusing first on the continent-wide structure and then, in more detail, on eastern different regions.

3.1 Continental model

As observed in many other studies, the average isotropic shear velocity V_S in the shallow upper mantle beneath North America (NA) is high compared to the global average, which contains contributions from large oceanic regions (Figure 7). The difference persists until ca. 270 km depth and then fades away, though, V_S remains slightly higher in NA than in the global average. Compared to the continental average, precambrian provinces like Wyoming, Yavapai, Mazatzal, Great Rhyolites and Grenville are characterized by slower velocities. The cordillera region shows the slowest velocities, close the global average as for ξ . Closer to the center of the continent, region like Slave, T.H.O, Juvenile arcs and orogens (e.g. Wopmay), Superior; show higher velocities with the Slave province characterized by a positive gradient above 100 km deep.

The average of ξ is higher than 1 (which means that $V_{SH} > V_{SV}$), but lower than the global average, the latter influenced by the strong $\xi > 1$ oceanic signature. Both trends are similar with depth, but the maximum in ξ is slightly deeper than in the global average and the change from $V_{SH} > V_{SV}$ to $V_{SH} < V_{SV}$ is reached at ca. 420km. This feature was already present in the global model, and perturbations below that depth are $\pm 1\%$ So I dont think

the model adds more informations compared to SEMucb. Regions showing highest ξ values

3.2 Beneath the craton

Our study confirms the presence of a thick lithospheric root in the craton with faster than average V_S down to 250km depth, with highest velocities, ca. 4.8 km.s^{-1} , located at depths shallower than 150km (e.g. Figure 8).

Laterally, the cratonic root in V_S coincides roughly with precambrian aged crust (see Figure 5 at from 60 to 150km deep) The western edge of the craton follows the RMF, instead of the western breakup line (See the red thin line in Figure 1 which coincides with RMF in Canada, but is diverging westward in the U.S.). While the eastern/south-esatern coincides with the Llano-Grenville Front (See the blue thin line in Figure 1). The northern part ends at the coastline of the Arctic ocean including the arctic archipelago and Greenland.

These lateral edges are well observed down to 150km depth. Below that, the cratonic root retracts toward the center of the archaeen continent and is still present beneath Slave, Hearne/Rae and western Superior cratons as shown in Figure 9. Everywhere within the craton, a negative gradient of

V_S is observed, marking the base of the lithosphere, with a minimum of $\sim 4.6 \text{ km.s}^{-1}$ reached at $\sim 300 \text{ km}$ depth. While the base of the lithosphere (and top of the low velocity zone- LVZ) shows strong topography, the bottom of the LVZ appears largely flat, in particular under the Slave, Hearne/Rae and western Superior cratons. As observed in Babuška et al. (1998), Gung et al. (2003), Yuan et al. (2014), there are large lateral variations ξ down to $\sim 200 \text{ km}$ depth, with regions of reduced radial anisotropy, in contrast to the more uniform, positive $d\ln(\xi)$ structure in this depth range in the oceans. Generally, ξ always appear higher than 1. Around 100 km negative $d\ln(\xi)$ compared to the isotropic case are observed in Mexico, at the southern part of Florida, the southern part of the Superior craton comprising the Mid Continental rifting, the southern part of the Granit Rhyolite Province comprising the Failed Rifting area and finally beneath Baffin Island.

3.2.1 Wyoming

h

The Archaean aged Wyoming craton does not show as high anomalies as within the craton nucleus as shown in figure 5. It is split into 2 distinctive part. A western part showing low velocities influenced by the active tectonic

with a radially positive gradient. In contrast with the eastern part showing higher velocities with a radially negative then positive gradient. The depth of negative gradient's minima is variable, from 70 (western part) to 250km (eastern part) deep. The separation between the two areas coincides with the RMF.

3.2.2 Slave

The Archaean aged Slave craton shows typical lithospheric craton signatures with higher than average velocities as shown in figure 5 and in figure 8. It shows in the entire region a positive velocity gradient with a maximum of ca. 4.8 km.s^{-1} associated with a maximum of ξ at ca. 150km deep. Deeper, a negative gradient is observed with a minimum of ca. 4.6 km.s^{-1} at ca. 250km deep. The topography of the extrema appears flat. (Est ce que c'est une caractéristique d'un craton stable non déformé?) Although the Slave lithosphere shows highest velocities at 150km, above 100km velocities are slightly higher than the continental average ($d\ln(V_S) < 4\%$).

3.2.3 Superior Craton

In our model, the Superior craton can be split in two parts: The western part showing typical cratonic structures while the eastern part shows slower velocities at all depths. Below 150km , velocity anomalies are below 2% (almost 0%).

Western part The Archaean aged Superior craton shows typical lithospheric craton signatures with higher than average velocities as shown in figure 5 and in figure 8. It shows in the entire region a positive velocity gradient with a maximum of ca. $4.8\text{km}\cdot\text{s}^{-1}$ associated with a maximum of ξ at ca. 150km deep.

Deeper a negative gradient is observed with a minimum of ca. $4.6\text{km}\cdot\text{s}^{-1}$ at ca. 250km deep. Opposed to the Slave craton, the topography of the extrema is variable. From SW to NE, the core of maximum velocity can reach between 70 and 150km of thickness. Beneath the maximum velocity region of ca. 150km the negative gradient appears steeper than beneath the 70km one, while the topography of the deeper positive gradient appears flat. At the south-eastern part of the western Superior, close the Mid-Lithospheric rift, we can observe the thinning of the cratonic lithosphere when crossing the

Grenville front. The band of minimum velocity within the cratonic root has similar amplitudes, in terms of velocity, than beneath the younger lithosphere but at shallower depths between 100 and 150km. Following the Great Meteor track built by Heaman and Kjarsgaard (2000), which crosses the Superior craton, it is interesting to note that the low velocity channel beneath the base of the lithosphere shows lower velocities than usually observed beneath the other Archaean cratons. This slow anomaly corresponds to the V-shape dent, or divot, observed by van der Lee and Nolet (1997) who explained the feature by the presence of water in the mantle. We observe at 250km that the slow anomaly goes further inland and crosses the Superior Craton northward until the Hudson bay following the GMT.

Eastern part Compared to its western part, the structure here shows differences as shown in figure 9. Fast velocities are present down to 150km deep but are slower. The negative gradient is steeper and the minimum is radially thicker. However at the center, the minimum channel is not continuous and shows higher (still slower than the center of the western Superior) velocities.

3.2.4 Trans Hudson Orogen

The Trans Hudson Orogen (THO) is a belt of Paleo-Proterozoic aged region. It refers to a major tectonic event (between 2.0 to 1.8Ga) that welded Archaean blocks to form the Laurentia Craton. It is interesting to notice that at shallower depths than 100km, the proterozoic THO (including the Sask craton) which welded the Superior and Rae/Hearne cratons, shows lighter (i.e, +4% compared to +8%) positive anomalies than its archaean surrounding. While most of the proterozoic root start to thin out at 150km, the THO at the vicinity of the hudson bay shows as high anomalies as Rae/Hearne and Superior areas. Je suis en train de construire des profils le long de THO pour voir!

3.2.5 Yavapai/Mazatzal/Granit-Rhyolite region

Yavapai/Mazatzal/Granit-Rhyolite orogens from 1.8 to 1.6 Ga represent zones of accretion for Proterozoic material and mark the amalgamation of the archean cores. (Hoffman 1988)

West to the RMF, the region shows low velocities influenced by the active tectonic with a radially positive gradient. The north eastern part shows velocity anomalies slightly lower than the Archaean nucleus. Velocity maxima

of 4.8 km.s^{-1} are located shallower than 100 km . Below, the radially negative gradient is observed and shows the same characteristic than the eastern Superior craton. It is interesting to note that, beneath Nebraska and Kansas, a high velocity anomaly of about 4.7 km.s^{-1} is present until ca. 170 km (while it is 120 km in most of the region) where cretaceous aged kimberlites are sampled. These kimberlites indicate a lithosphere thickness of about 160 km and have been affected by asthenospheric upwelling related to the Mid-Continent Rift System. (Griffin et al. 2004)

3.3 Surrounding oceanic

This section needs to be redone...

Our inversion is focusing on the continental part, as shown in our spatial parameterization (i.e. see figure 3) where the region is sampled by data. Except the oceanic borders of NA, further away, the structure has not been updated from SEMucb_wm1 (French and Romanowicz 2014).

3.3.1 Eastern Passive margin

As in Schaeffer and Lebedev (2014), Yuan et al. (2014), James et al. (2014), Silveira and Stutzmann (2002), Mocquet and Romanowicz (1990), we observe

along the negative anomaly structure following the Appalachian continental shelf, a stretched positive anomaly structure from the Suwanne terrane in Florida to the Avalonian terranes of New-Scotland. At 60km it is made of several blocks of at most +3% anomalies embedded in a +2% structure. At 150km , the structure is split into 2 blocks by a slow anomaly comprising both the Great Meteor (GMT) and Bermuda tracks, and further southeast, the Low Velocities Fingers (LVF) observed in French et al. (2013).

Such structure would correspond to late proterozoic gondwanian continental terranes that formed during the Pan African orogenesis (Kennedy 1964) and remained attached to the North American margin during the opening of the Atlantic ocean. (e.g. Thomas 2006) On the continental shelf, authors (e.g. O'Brien et al. 1983, Nance et al. 2002) identified the west Avalonian terranes of pan-african affinity as in Florida (see Smith 1982) that might have been underlaid by a thin (ca. 100km) lithosphere before the Pangaea assembling. (McKenzie et al. 2015)

Fast anomalies are observed beneath the whole gulf of Mexico down to 150km deep. Despite the proximity with pan-african lithosphere, such high velocity anomalies represent older than $ca.150\text{Ma}$ oceanic lithosphere. (Müller et al. 2008, Pindell and Kennan 2009) – No Magnetic anomalies

recorded as in Pan African, Oceanic seafloor according to Pindel –

3.3.2 The Great Meteor track

Our model images a slow velocity anomaly in agreement with the reconstruction of the Great Meteor Track (thin red line in figure 5) proposed by Heaman and Kjarsgaard (2000). Below 100km the pan african lithosphere is cut in two by a slow velocity anomaly beneath the New England seamounts (youngest part of the GMT). Further East, the slow anomaly follows the GMT crossing the continental shelf, Appalachian and Grenville orogens down to 200km. This slow anomaly corresponds to the V-shape dent, or divot, observed by van der Lee and Nolet (1997) who explained the feature by the presence of water in the mantle. We observe at 250km that the slow anomaly goes further inland and crosses the Superior Craton northward until the Hudson bay following the GMT. See the cross section along the re-built GMT in figure 10.

Heaman and Kjarsgaard (2000), based on $U - Pb$ perovskite age determinations of kimberlites, proposed a progressive southeastward younging of kimberlite magmatism throughout much of eastern North America. Considering it as a strong support for small volume mantle melting that have

occurred along the continental portion of the Mesozoic Great Meteor mantle plume hotspot track initiated during the opening of the North Atlantic Ocean at about 200Ma. (See figure 4. in Heaman and Kjarsgaard 2000)

Davies (1994) described a process of thermo-mechanical erosion which involves heating-softening of the lithospheric base by a plume tail, followed by mechanical removal of the material due to convective transfer. (Rondenay et al. 2000)

References

- Abt, D. L., Fischer, K. M., French, S. W., Ford, H. A., Yuan, H., and Romanowicz, B. (2010). North american lithospheric discontinuity structure imaged by PsandSpreceiver functions. *Journal of Geophysical Research*, 115(B9).
- Babuška, V., Montagner, J.-P., Plomerová, J., and Girardin, N. (1998). Age-dependent large-scale fabric of the mantle lithosphere as derived from surface-wave velocity anisotropy. In *Geodynamics of Lithosphere & Earths Mantle*, pages 257–280. Springer.
- Backus, G. E. (1962). Long-wave elastic anisotropy produced by horizontal

- layering. *Journal of Geophysical Research*, 67(11):4427–4440.
- Bassin, C., Laske, G., and Masters, G. (2000). The current limits of resolution for surface wave tomography in north america. *EOS Trans AGU*.
- Bedle, H. and van der Lee, S. (2009). Svelocity variations beneath North America. *Journal of Geophysical Research*, 114(B7).
- Bostock, M. (1998). Mantle stratigraphy and evolution of the slave province. *Journal of Geophysical Research: Solid Earth*, 103(B9):21183–21200.
- Bozdağ, E., Peter, D., Lefebvre, M., Komatitsch, D., Tromp, J., Hill, J., Podhorszki, N., and Pugmire, D. (2016). Global adjoint tomography: First-generation model. *Geophysical Journal International*, page ggw356.
- Burdick, S., Van der Hilst, R. D., Vernon, F. L., Martynov, V., Cox, T., Eakins, J., Karasu, G. H., Tylell, J., Astiz, L., and Pavlis, G. L. (2014). Model update january 2013: Upper mantle heterogeneity beneath north america from travel-time tomography with global and usarray trans-portable array data. *Seismological Research Letters*, 85(1):77–81.
- Calò, M., Bodin, T., and Romanowicz, B. (2016). Layered structure in the

upper mantle across North America from joint inversion of long and short period seismic data. *Earth and Planetary Science Letters*, 449:164–175.

Capdeville, Y. and Marigo, J.-J. (2008). Shallow layer correction for spectral element like methods. *Geophysical Journal International*, 172(3):1135–1150.

Cleary, J. and Hales, A. L. (1966). An analysis of the travel times of p waves to north american stations, in the distance range 32 to 100. *Bulletin of the Seismological Society of America*, 56(2):467–489.

Cupillard, P., Delavaud, E., Burgos, G., Festa, G., Villette, J.-P., Capdeville, Y., and Montagner, J.-P. (2012). RegSEM: a versatile code based on the spectral element method to compute seismic wave propagation at the regional scale. *Geophysical Journal International*, 188(3):1203–1220.

Davies, G. F. (1994). Thermomechanical erosion of the lithosphere by mantle plumes. *Journal of Geophysical Research: Solid Earth*, 99(B8):15709–15722.

Debayle, E. and Ricard, Y. (2012). A global shear velocity model of the upper mantle from fundamental and higher Rayleigh mode measurements. *Journal of Geophysical Research: Solid Earth*, 117(B10).

Deschamps, F., Lebedev, S., Meier, T., and Trampert, J. (2008). Stratified seismic anisotropy reveals past and present deformation beneath the east-central United States. *Earth and Planetary Science Letters*, 274(3-4):489–498.

Fischer, K. M., Ford, H. A., Abt, D. L., and Rychert, C. A. (2010). The lithosphere-asthenosphere boundary. *Annu. Rev. Earth Planet. Sci.*, 38(1):551–575.

Ford, H. A., Long, M. D., and Wirth, E. A. (2016). Midlithospheric discontinuities and complex anisotropic layering in the mantle lithosphere beneath the wyoming and superior provinces. *Journal of Geophysical Research: Solid Earth*, 121(9):6675–6697.

French, S., Lekic, V., and Romanowicz, B. (2013). Waveform tomography reveals channeled flow at the base of the oceanic asthenosphere. *Science*, 342(6155):227–230.

French, S. W. and Romanowicz, B. A. (2014). Whole-mantle radially anisotropic shear velocity structure from spectral-element waveform tomography. *Geophysical Journal International*, 199(3):1303–1327.

Grand, S. P. and Helmberger, D. V. (1984). Upper mantle shear structure of North America. *Geophysical Journal International*, 76(2):399–438.

Griffin, W., O'Reilly, S. Y., Doyle, B., Pearson, N., Coopersmith, H., Kivi, K., Malkovets, V., and Pokhilenko, N. (2004). Lithosphere mapping beneath the north american plate. *Lithos*, 77(1):873–922.

Gung, Y., Panning, M., and Romanowicz, B. (2003). Global anisotropy and the thickness of continents. *Nature*, 422(6933):707–711.

Heaman, L. and Kjarsgaard, B. (2000). Timing of eastern north american kimberlite magmatism: continental extension of the great meteor hotspot track? *Earth and Planetary Science Letters*, 178(3):253–268.

Herrin, E. and Taggart, J. (1968). Regional variations in p travel times. *Bulletin of the Seismological Society of America*, 58(4):1325–1337.

Hoffman, P. F. (1988). United plates of America, the birth of a craton: Early proterozoic assembly and growth of laurentia. *Annu. Rev. Earth Planet. Sci.*, 16(1):543–603.

James, E. K., Dalton, C. A., and Gaherty, J. B. (2014). Rayleigh wave

phase velocities in the atlantic upper mantle. *Geochemistry, Geophysics, Geosystems*, 15(11):4305–4324.

Kennedy, W. (1964). The structural differentiation of africa in the pan-african (± 500 my) tectonic episode. *Leeds Univ. Res. Inst. Afr. Geol. Annu. Rep*, 8:48–49.

King (2005). Archean cratons and mantle dynamics. *Earth and Planetary Science Letters*, 234(1-2):1–14.

Komatitsch, D. (2002). The spectral-element method, beowulf computing, and global seismology. *Science*, 298(5599):1737–1742.

Kustowski, B., Ekstrm, G., and Dziewoński, A. M. (2008). Anisotropic shear-wave velocity structure of the earth's mantle: A global model. *J. Geophys. Res.*, 113(B6).

Lee, C.-T. A., Luffi, P., and Chin, E. J. (2011). Building and destroying continental mantle. *Annu. Rev. Earth Planet. Sci.*, 39(1):59–90.

Lekić, V. and Romanowicz, B. (2011). Inferring upper-mantle structure by full waveform tomography with the spectral element method. *Geophysical Journal International*, 185(2):799–831.

- Levin, V., Menke, W., and Park, J. (1999). Shear wave splitting in the appalachians and the urals- a case for multilayered anisotropy. *Journal of Geophysical Research*, 104(17):975–17.
- Li, X.-D. and Romanowicz, B. (1995). Comparison of global waveform inversions with and without considering cross-branch modal coupling. *Geophysical Journal International*, 121(3):695–709.
- Li, X.-D. and Romanowicz, B. (1996). Global mantle shear velocity model developed using nonlinear asymptotic coupling theory. *J. Geophys. Res.*, 101(B10):22245–22272.
- Love, A. E. H. (2013). *A treatise on the mathematical theory of elasticity*. Cambridge university press.
- Marone, F., Gung, Y., and Romanowicz, B. (2007). Three-dimensional radial anisotropic structure of the north american upper mantle from inversion of surface waveform data. *Geophysical Journal International*, 171(1):206–222.
- Marone, F. and Romanowicz, B. (2007). The depth distribution of azimuthal anisotropy in the continental upper mantle. *Nature*, 447(7141):198–201.
- Masson, Y., Cupillard, P., Capdeville, Y., and Romanowicz, B. (2013). On

the numerical implementation of time-reversal mirrors for tomographic imaging. *Geophysical Journal International*, 196(3):1580–1599.

Masson, Y. and Romanowicz, B. (2016). Box tomography: Localised imaging of remote targets buried in an unknown medium, a step forward for understanding key structures in the deep earth. *Geophysical Journal International*.

Masson, Y. and Romanowicz, B. (2017). Fast computation of synthetic seismograms within a medium containing remote localized perturbations: a numerical solution to the scattering problem. *Geophysical Journal International*, 208(2):674–692.

McKenzie, D., Daly, M. C., and Priestley, K. (2015). The lithospheric structure of pangea. *Geology*, 43(9):783–786.

Mégnin, C. and Romanowicz, B. (1999). The effects of the theoretical formalism and data selection on mantle models derived from waveform tomography. *Geophysical Journal International*, 138(2):366–380.

Mégnin, C. and Romanowicz, B. (2000). The three-dimensional shear velocity structure of the mantle from the inversion of body, surface and higher-mode waveforms. *Geophysical Journal International*, 143(3):709–728.

Mochizuki, E. (1986). The free oscillations of an anisotropic and heterogeneous earth. *Geophysical Journal International*, 86(1):167–176.

Mocquet, A. and Romanowicz, B. (1990). Three-dimensional structure of the upper mantle beneath the atlantic ocean inferred from longperiod rayleigh waves, ii. *Inversion. J. Geophys. Res.*, 95:6787–6798.

Montagner, J.-P. and Anderson, D. L. (1989). Petrological constraints on seismic anisotropy. *Physics of the Earth and Planetary Interiors*, 54(1-2):82–105.

Müller, R. D., Sdrolias, M., Gaina, C., and Roest, W. R. (2008). Age, spreading rates, and spreading asymmetry of the world's ocean crust. *Geochemistry, Geophysics, Geosystems*, 9(4).

Nance, R. D., Murphy, J. B., and Keppie, J. D. (2002). A cordilleran model for the evolution of avalonia. *Tectonophysics*, 352(1):11–31.

Nettles, M. and Dziewoński, A. M. (2008). Radially anisotropic shear velocity structure of the upper mantle globally and beneath North America. *J. Geophys. Res.*, 113(B2).

O'Brien, S., Wardle, R., and King, A. (1983). The avalon zone: a pan-

african terrane in the appalachian orogen of canada. *Geological Journal*, 18(3):195–222.

Panning, M. and Romanowicz, B. (2006). A three-dimensional radially anisotropic model of shear velocity in the whole mantle. *Geophysical Journal International*, 167(1):361–379.

Pindell, J. L. and Kennan, L. (2009). Tectonic evolution of the gulf of mexico, caribbean and northern south america in the mantle reference frame: an update. *Geological Society, London, Special Publications*, 328(1):1–55.

Porritt, R. W., Allen, R. M., and Pollitz, F. F. (2014). Seismic imaging east of the rocky mountains with usarray. *Earth and Planetary Science Letters*, 402:16–25.

Porritt, R. W., Miller, M. S., and Darbyshire, F. A. (2015). Lithospheric architecture beneath hudson bay. *Geochemistry, Geophysics, Geosystems*, 16(7):2262–2275.

Poupinet, G. (1979). On the relation between p-wave travel time residuals and the age of continental plates. *Earth and Planetary Science Letters*, 43(1):149–161.

Rader, E., Emry, E., Schmerr, N., Frost, D., Cheng, C., Menard, J., Yu, C.-Q., and Geist, D. (2015). Characterization and petrological constraints of the midlithospheric discontinuity. *Geochemistry, Geophysics, Geosystems*, 16(10):3484–3504.

Ritsema, J., Deuss, A., van Heijst, H. J., and Woodhouse, J. H. (2010). S40rts: a degree-40 shear-velocity model for the mantle from new Rayleigh wave dispersion, teleseismic traveltimes and normal-mode splitting function measurements. *Geophysical Journal International*, 184(3):1223–1236.

Romanowicz, B. (1987). Multiplet-multiplet coupling due to lateral heterogeneity: asymptotic effects on the amplitude and frequency of the earth's normal modes. *Geophysical Journal International*, 90(1):75–100.

Romanowicz, B. A. (1979). Seismic structure of the upper mantle beneath the United States by three-dimensional inversion of body wave arrival times. *Geophysical Journal International*, 57(2):479–506.

Romanowicz, B. A., Panning, M. P., Gung, Y., and Capdeville, Y. (2008). On the computation of long period seismograms in a 3-D earth using normal mode based approximations. *Geophysical Journal International*, 175(2):520–536.

Rondenay, S., Bostock, M. G., Hearn, T. M., White, D. J., and Ellis, R. M. (2000). Lithospheric assembly and modification of the se canadian shield: Abitibi-grenville teleseismic experiment. *Journal of Geophysical Research: Solid Earth*, 105(B6):13735–13754.

Schaeffer, A. and Lebedev, S. (2014). Imaging the north american continent using waveform inversion of global and USArray data. *Earth and Planetary Science Letters*, 402:26–41.

Schaeffer, A. J. and Lebedev, S. (2013). Global shear speed structure of the upper mantle and transition zone. *Geophysical Journal International*, 194(1):417–449.

Shapiro, N. M. and Ritzwoller, M. H. (2002). Monte-Carlo inversion for a global shear-velocity model of the crust and upper mantle. *Geophysical Journal International*, 151(1):88–105.

Sigloch, K. (2011). Mantle provinces under North America from multifrequencyPwave tomography. *Geochemistry, Geophysics, Geosystems*, 12(2):n/a–n/a.

Silveira, G. and Stutzmann, E. (2002). Anisotropic tomography of the atlantic ocean. *Physics of the Earth and Planetary Interiors*, 132(4):237–248.

Smith, D. L. (1982). Review of the tectonic history of the florida basement. *Tectonophysics*, 88(1-2):1–22.

Su, W.-j., Woodward, R. L., and Dziewonski, A. M. (1994). Degree 12 model of shear velocity heterogeneity in the mantle. *Journal of Geophysical Research: Solid Earth*, 99(B4):6945–6980.

Tarantola, A. (2005). *Inverse problem theory and methods for model parameter estimation*. siam.

Tarantola, A. and Valette, B. (1982). Generalized nonlinear inverse problems solved using the least squares criterion. *Reviews of Geophysics*, 20(2):219–232.

Thomas, W. A. (2006). Tectonic inheritance at a continental margin. *GSA today*, 16(2):4–11.

Thybo, H. and Perchu, E. (1997). The seismic 8 discontinuity and partial melting in continental mantle. *Science*, 275(5306):1626–1629.

Unser, M., Aldroubi, A., and Eden, M. (1993a). B-spline signal processing. i. theory. *IEEE transactions on signal processing*, 41(2):821–833.

Unser, M., Aldroubi, A., and Eden, M. (1993b). B-spline signal processing. ii.

- efficiency design and applications. *IEEE transactions on signal processing*, 41(2):834–848.
- Valentine, A. P. and Trampert, J. (2016). The impact of approximations and arbitrary choices on geophysical images. *Geophysical Journal International*, 204(1):59–73.
- van der Lee, S. and Frederiksen, A. (2005). Surface wave tomography applied to the north american upper mantle. In *Seismic Earth: Array Analysis of Broadband Seismograms*, pages 67–80. Wiley-Blackwell.
- van der Lee, S. and Nolet, G. (1997). Upper mantleSvelocity structure of North America. *Journal of Geophysical Research: Solid Earth*, 102(B10):22815–22838.
- Wang, Z. and Dahlen, F. A. (1995). Spherical-spline parameterization of three-dimensional earth models. *Geophysical Research Letters*, 22(22):3099–3102.
- Whitmeyer, S. J. and Karlstrom, K. E. (2007). Tectonic model for the proterozoic growth of north america. *Geosphere*, 3(4):220–259.
- Woodhouse, J. H. and Dziewonski, A. M. (1984). Mapping the upper man-

- tle: Three-dimensional modeling of earth structure by inversion of seismic waveforms. *Journal of Geophysical Research: Solid Earth*, 89(B7):5953–5986.
- Yuan, H., French, S., Cupillard, P., and Romanowicz, B. (2014). Lithospheric expression of geological units in central and eastern North America from full waveform tomography. *Earth and Planetary Science Letters*, 402:176–186.
- Yuan, H. and Romanowicz, B. (2010). Lithospheric layering in the north american craton. *Nature*, 466(7310):1063–1068.
- Yuan, H., Romanowicz, B., Fischer, K. M., and Abt, D. (2011). 3-D shear wave radially and azimuthally anisotropic velocity model of the north american upper mantle. *Geophysical Journal International*, 184(3):1237–1260.
- Zhou, Y., Dahlen, F., Nolet, G., and Laske, G. (2005). Finite-frequency effects in global surface-wave tomography. *Geophysical Journal International*, 163(3):1087–1111.
- Zhu, H., Bozdağ, E., and Tromp, J. (2015). Seismic structure of the eu-

ropean upper mantle based on adjoint tomography. *Geophysical Journal International*, 201(1):18–52.

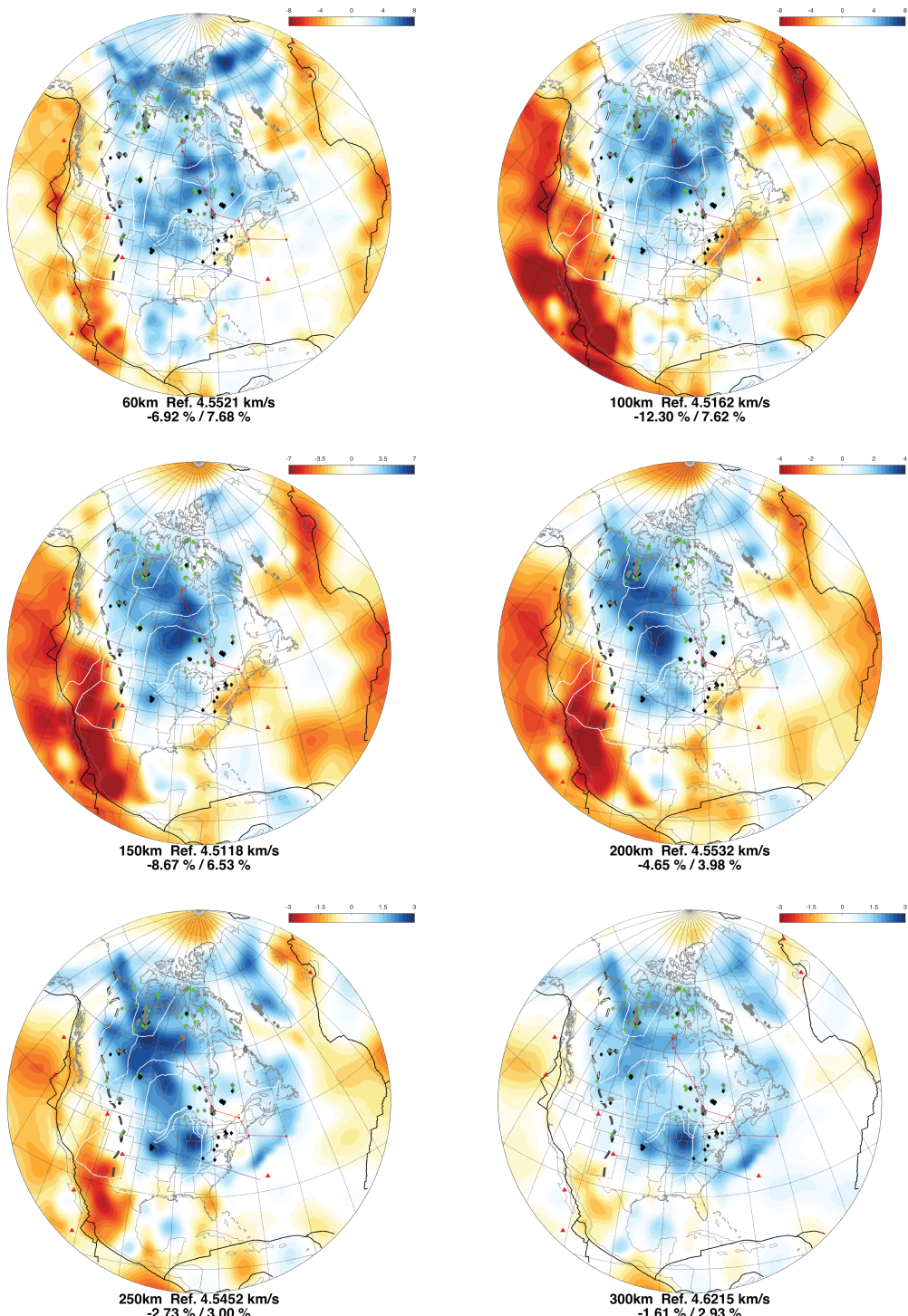
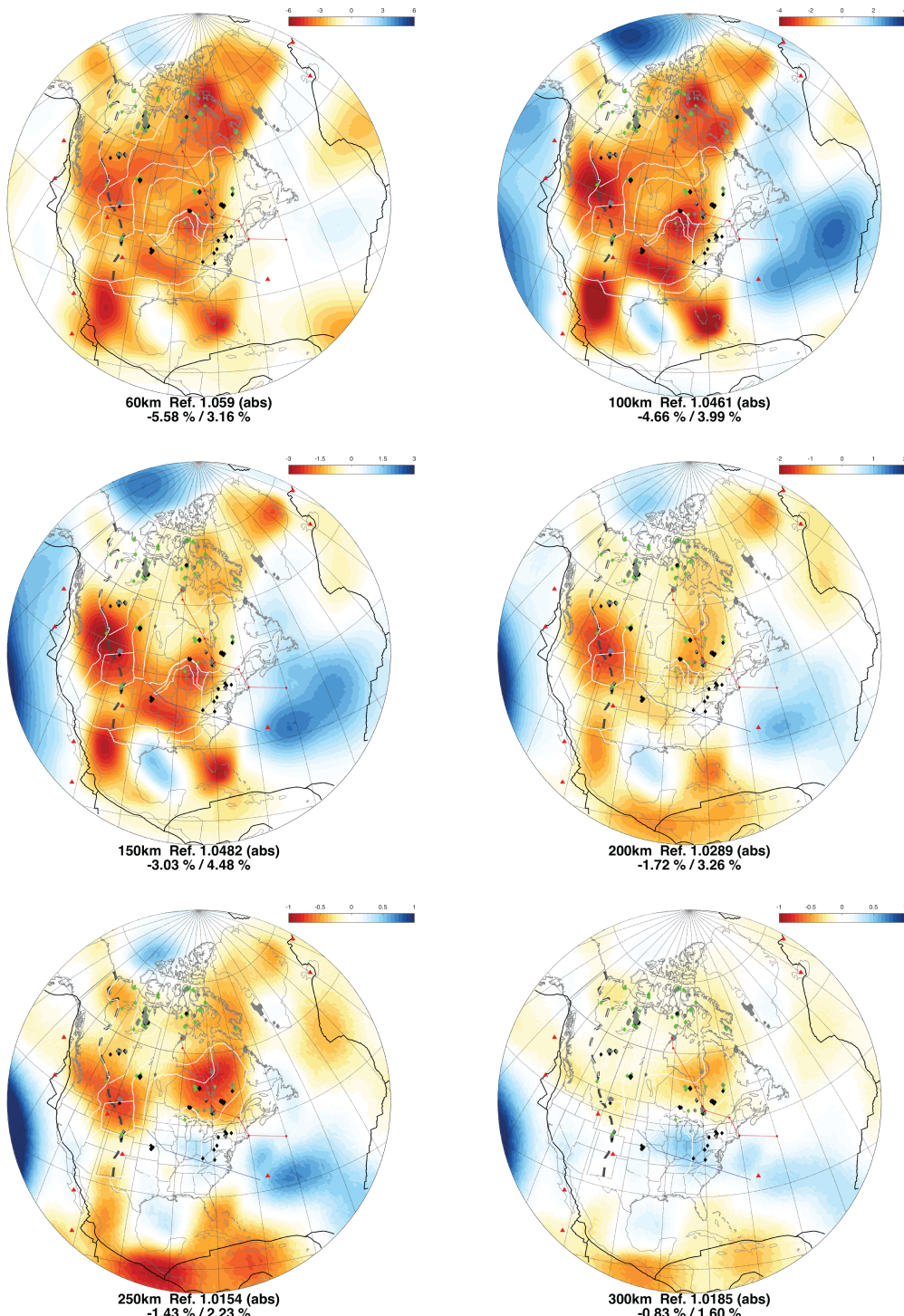


Figure 5: 3D isotropic shear wave velocity structure of the continent. Map views are shown from 60 km down to 300 km, shown as variations with respect to the global mean (thick red line in Figure 7).



52
 Figure 6: 3D isotropic radial anisotropy structure of the continent. Map views are shown from 60 km down to 300 km, shown as variations with respect to the regional mean (thick red line in Figure 7).

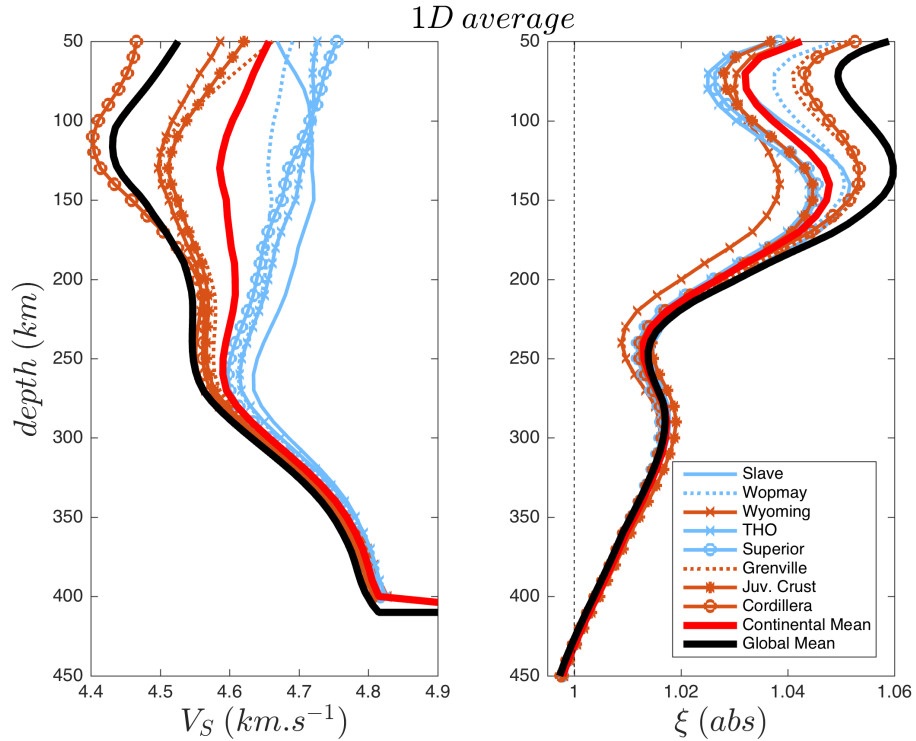


Figure 7: 1D average depth profiles for isotropic shear velocity (left) and radial anisotropy (right), for the SEMucb_wm1 global model (thick black), the continental average (thick red); and depth profiles for different regions in the model (see legend and Figure 1). The continental average is always higher than the global average in terms of V_S , while for ξ , they are similar deeper than 250 km.

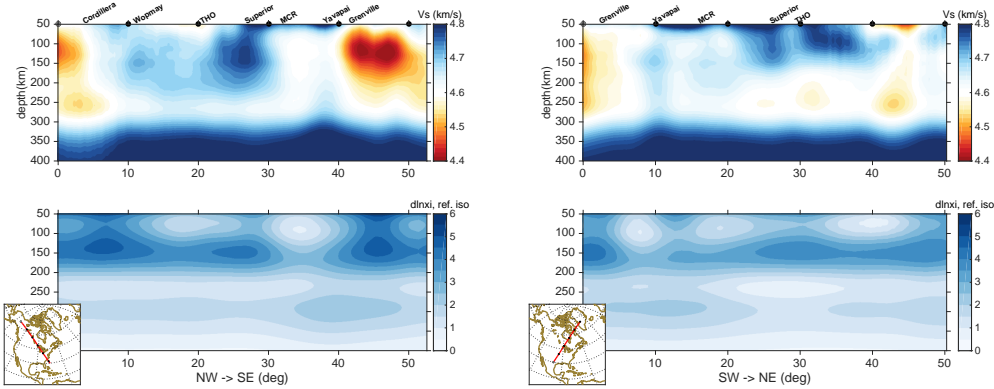


Figure 8: Cross Section of the lithospheric core

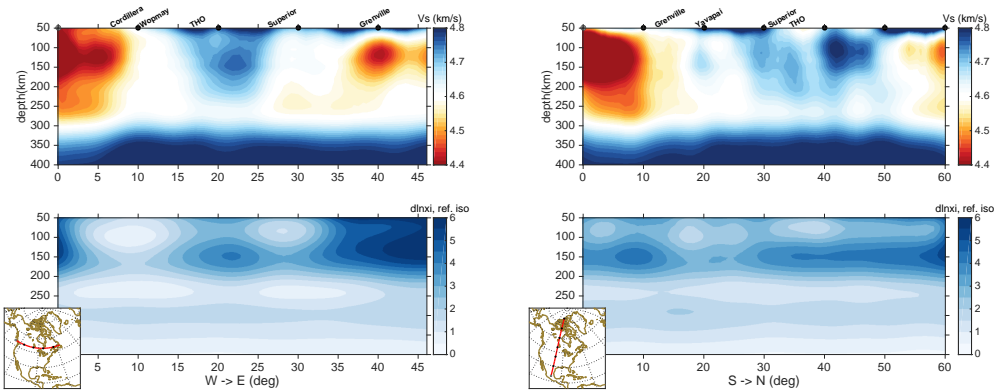


Figure 9: Cross Section of the lithospheric core showing the core retraction

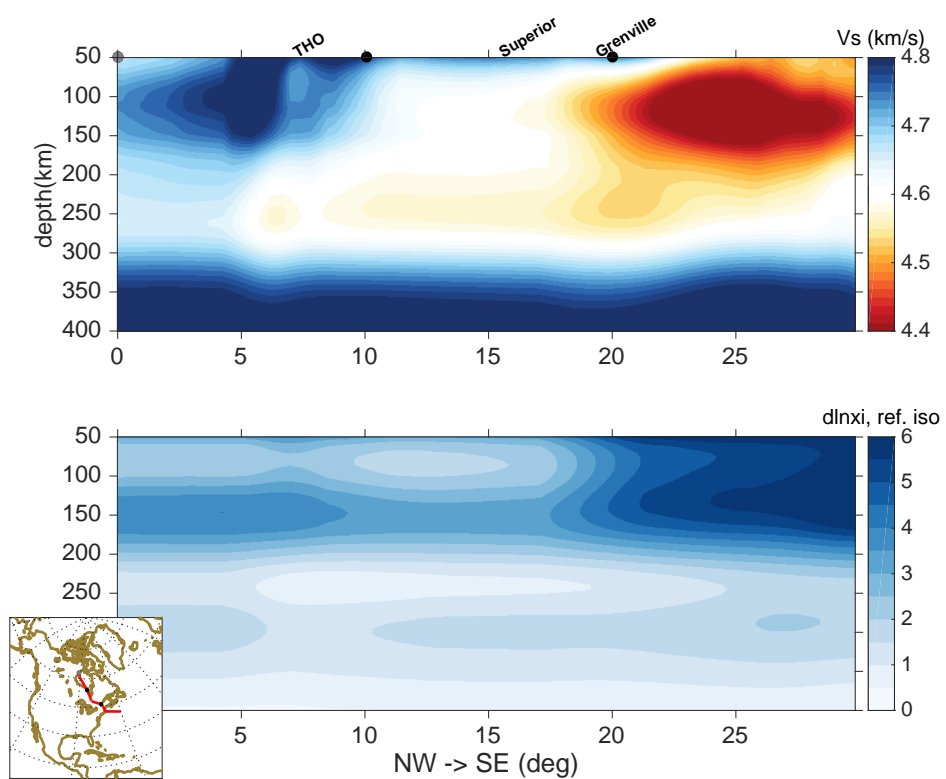


Figure 10: Cross Section of the lithosphere along the Great Meteor track based on Heaman and Kjarsgaard (2000) construction